catalysts

MDPI

Article

Sunlight-Driven Synthesis of $TiO_2/(MA)_2SnCl_4$ Nanocomposite Films for Enhanced Photocatalytic Degradation of Organic Pollutants

Abdellah Kaiba [1], Amani M. Alansi [2], Ali Oubelkacem [3], Ilyas Chabri [3], Salah T. Hameed [4], Naveed Afzal [5], Mohsin Rafique [5] and Talal F. Qahtan [1,*]

[1] Department of Physics, College of Science and Humanities in Al-Kharj, Prince Sattam bin Abdulaziz University, Al-Kharj 11942, Saudi Arabia; a.kaiba@psau.edu.sa
[2] Chemistry Department, College of Science, Taiz University, Taiz 12372, Yemen; mn.alansi2016@gmail.com
[3] Laboratory of Materials Physics and Systems Modelling, (LP2MS), Physics Department, Faculty of Science, University Moulay Ismail, Meknes 50050, Morocco; a.oubelkacem@umi.ac.ma (A.O.); ilyasmath9@gmail.com (I.C.)
[4] Physics Department, Faculty of Education, Taiz University, Taiz 12372, Yemen; salah1phy@gmail.com
[5] Centre for Advanced Studies in Physics, GC University, Lahore 54000, Pakistan; naveedafzal@gcu.edu.pk (N.A.); mohsinrafique@gcu.edu.pk (M.R.)
* Correspondence: t.qahtan@psau.edu.sa or tfqahtan@gmail.com

Abstract: In this study, a $TiO_2/(MA)_2SnCl_4$ nanocomposite film was synthesized using a sustainable, sunlight-driven approach, demonstrating enhanced photocatalytic performance for environmental remediation. TiO_2 nanoparticles (TiO_2-NPs) were dispersed in ethanol and mixed with a methylammonium (MA) and $SnCl_2$ precursor solution, followed by drop-casting onto a glass substrate and exposure to direct sunlight for 2 h. Sunlight served as an energy source, facilitating in situ structural modifications and leading to the formation of a well-integrated $TiO_2/(MA)_2SnCl_4$ hybrid structure, where TiO_2 was effectively encapsulated. Characterization revealed a band gap reduction from 3.1 eV (TiO_2-NPs) to 2.6 eV in the nanocomposite, extending light absorption into the visible range. The formation of Sn–O–Ti interactions enhanced charge separation, minimized electron–hole recombination, and improved charge carrier dynamics. Photocatalytic degradation tests using methylene blue (MB) under sunlight showed that the nanocomposite film achieved 90% MB degradation within 60 min, outperforming TiO_2-NPs, which achieved only 75% degradation. The presence of oxygen vacancies (OVs) generated during sunlight exposure further enhanced photocatalytic efficiency by acting as charge traps and reaction sites. This study introduces a green synthesis strategy leveraging sunlight as a renewable energy source, marking the first integration of $(MA)_2SnCl_4$ with TiO_2-NPs for enhanced photocatalysis. The synergistic effects of extended visible-light absorption, defect engineering, and efficient charge separation make $TiO_2/(MA)_2SnCl_4$ nanocomposite films a scalable, cost-effective solution for water purification applications, offering a promising solar-driven approach to addressing global water contamination challenges.

Keywords: photocatalysis; $TiO_2/(MA)_2SnCl_4$ nanocomposite film; sunlight-driven synthesis; visible light absorption; environmental remediation

check for updates

Academic Editors: Feng Wang, Xiyu Cheng and Jianhua Hu

Received: 22 December 2024
Revised: 20 January 2025
Accepted: 23 January 2025
Published: 24 February 2025

Citation: Kaiba, A.; Alansi, A.M.; Oubelkacem, A.; Chabri, I.; Hameed, S.T.; Afzal, N.; Rafique, M.; Qahtan, T.F. Sunlight-Driven Synthesis of $TiO_2/(MA)_2SnCl_4$ Nanocomposite Films for Enhanced Photocatalytic Degradation of Organic Pollutants. *Catalysts* **2025**, *15*, 214. https://doi.org/10.3390/catal15030214

Copyright: © 2025 by the authors. Licensee MDPI, Basel, Switzerland. This article is an open access article distributed under the terms and conditions of the Creative Commons Attribution (CC BY) license (https://creativecommons.org/licenses/by/4.0/).

1. Introduction

The growing global demand for clean water has sparked extensive research into sustainable water purification technologies. Among these, photocatalysis has emerged as

a promising solution due to its ability to utilize sunlight to drive chemical reactions that degrade pollutants in water. Photocatalysis relies on photocatalyst materials that absorb light and generate reactive species capable of breaking down harmful contaminants. This process is not only effective but also environmentally friendly, leveraging solar energy, an abundant and renewable resource. By converting solar energy into chemical energy, photocatalysis offers a cost-effective and sustainable approach to water decontamination, making it a standout method for addressing water pollution on a large scale [1–5].

Titanium dioxide (TiO_2) is one of the most extensively researched photocatalysts, praised for its excellent oxidation capabilities, chemical stability, non-toxicity, and cost-effectiveness [6,7]. Despite these advantages, TiO_2 has a significant drawback, namely its relatively large band gap of around 3.2 eV (in the anatase form), which restricts its light absorption to the ultraviolet (UV) range, accounting for only about 5% of the solar spectrum [8,9]. As a result, the photocatalytic activity of TiO_2 under natural sunlight is limited, making it less effective for practical environmental applications. This narrow UV absorption hampers its ability to harness the full potential of solar energy, thus reducing its overall efficiency for photocatalytic processes.

To address the limitations of TiO_2, numerous strategies have been explored, including doping TiO_2 with metal or nonmetal ions, generating oxygen vacancies (OVs), and coupling TiO_2 with visible-light-responsive materials [10–13]. These modifications aim to extend the absorption of TiO_2 from the UV region into the visible range, thereby enhancing its photocatalytic performance under sunlight. Metal halide perovskites have emerged as promising candidates to improve photocatalytic efficiency due to their tunable band gaps, exceptional light absorption capabilities, and excellent charge carrier mobility [14,15]. Well-studied examples include methylammonium lead iodide ($CH_3NH_3PbI_3$) [16,17] and cesium lead bromide ($CsPbBr_3$) [18]. Despite their remarkable optoelectronic properties, their use in practical applications is limited due to concerns related to lead toxicity and chemical instability [19]. Methylammonium tin chloride ($(MA)_2SnCl_4$) is a non-toxic alternative to conventional lead-based perovskites, mitigating concerns about lead contamination. It offers multiple benefits, such as tunable band gaps, excellent visible light absorption, and high charge carrier mobility. Additionally, its ability to form a heterojunction with other semiconductors enhances photocatalytic efficiency by promoting effective charge separation and reducing recombination rates. These qualities make $(MA)_2SnCl_4$ an ideal material for significantly boosting the photocatalytic performance of TiO_2 [20,21].

There are different approaches to synthesizing TiO_2-based nanocomposites, including sol–gel methods, hydrothermal synthesis, chemical vapor deposition, and impregnation techniques [22,23]. However, many of these methods involve complex setups, high energy consumption, and the use of hazardous chemicals, which can hinder scalability and sustainability. This study employs a green, sunlight-driven synthesis method to create $TiO_2/(MA)_2SnCl_4$ nanocomposite films, offering a scalable and eco-friendly method for photocatalyst production without the need for complex, energy-intensive processes. Utilizing sunlight as the energy source, this in situ synthesis method aligns with green chemistry principles, presenting an effective, sustainable alternative for large-scale photocatalyst development.

The synthesis of the $TiO_2/(MA)_2SnCl_4$ nanocomposite involves dispersing TiO_2 nanoparticles (TiO_2-NPs) in ethanol and mixing them with a precursor solution containing methylammonium (MA) and $SnCl_2$. The resulting mixture is drop-cast onto a glass substrate and exposed to direct sunlight for 2 h, enabling the in situ formation of $(MA)_2SnCl_4$, which effectively encapsulates TiO_2-NPs. This hybrid structure combines the extended light absorption capabilities of Sn- and MA-incorporated phases with the efficient electron transport properties of TiO_2-NPs, enhancing photocatalytic degradation of pollutants under

sunlight. Additionally, the immobilization of the photocatalyst on a solid substrate offers ease of reuse, making it a practical solution for scalable environmental applications.

Photocatalytic tests using methylene blue (MB) degradation under sunlight demonstrated that the nanocomposite film achieved 90% degradation within 60 min, significantly surpassing the 75% degradation observed in TiO_2-NPs. This improvement is attributed to band gap reduction (2.6 eV vs. 3.1 eV for TiO_2-NPs), enhanced charge separation, and the presence of OVs that facilitate charge trapping and reactive species generation. The novelty of this study lies in the successful integration of Sn and MA into TiO_2-NPs through a simple, sunlight-driven synthesis approach, utilizing renewable solar energy to drive the formation and interaction of $(MA)_2SnCl_4$ with TiO_2. This cost-effective, scalable synthesis method provides a sustainable pathway for solar-driven water purification, demonstrating the potential of $TiO_2/(MA)_2SnCl_4$ nanocomposite films for practical environmental remediation applications.

2. Results and Discussion

Figure 1 presents Raman spectroscopy and SEM analysis of TiO_2-NPs and $TiO_2/(MA)_2SnCl_4$ nanocomposite films, highlighting the structural and morphological modifications induced by Sn and MA incorporation, as well as the integration of the $(MA)_2SnCl_4$ phase into the TiO_2-NPs framework. Raman spectra (Figure 1a,b) reveal that TiO_2-NPs exhibit distinct anatase peaks at 144, 197, 396, 515, and 640 cm^{-1}, confirming their high crystallinity [24]. In contrast, $TiO_2/(MA)_2SnCl_4$ shows broadened peaks with reduced intensity, suggesting Sn substitution within the TiO_2 lattice, TiO_2 encapsulation, and structural reorganization induced by $(MA)_2SnCl_4$ incorporation.

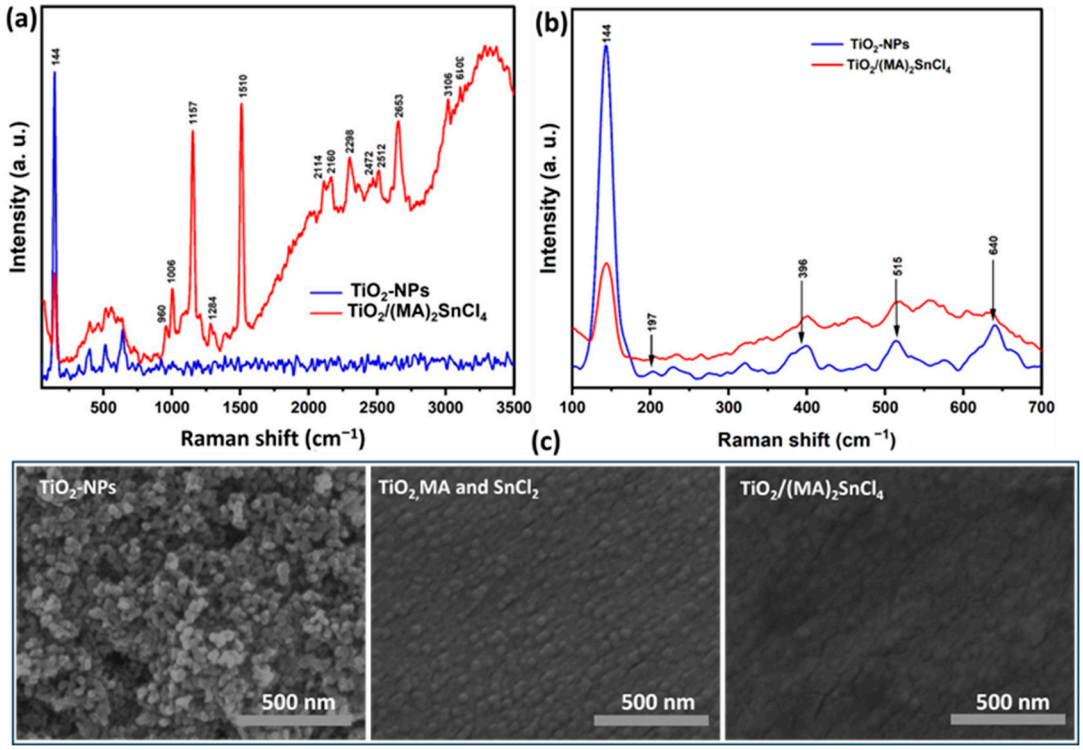


Figure 1. (**a**) Raman spectra of TiO_2-NPs and $TiO_2/(MA)_2SnCl_4$ nanocomposite. (**b**) Magnified Raman spectra in the low-frequency region (100–700 cm^{-1}), highlighting the weakening and broadening of char-acteristic TiO_2 peaks upon interaction with Sn and MA. (**c**) SEM images of TiO_2-NPs, TiO_2 mixed with MA and $SnCl_2$, and $TiO_2/(MA)_2SnCl_4$, illustrating the morphological transformation from agglomerated TiO_2 nanoparticles to a smooth and compact nanocomposite film, confirming en-capsulation and structural reorganization.

The appearance of additional peaks in the 1000–3500 cm^{-1} range, corresponding to C-H, N-H, and CH_3 vibrational modes from MA [25], confirms the successful integration of methylammonium into the hybrid structure, further validating the structural impact of $(MA)_2SnCl_4$ on TiO_2-NPs. The modifications in the low-frequency Raman region (144–640 cm^{-1}) suggest strong interactions between Sn and TiO_2, leading to lattice distortions, defect formation, and heterostructure evolution. These structural transformations, along with weakened TiO_2 vibrational modes, indicate that Sn incorporation and MA stabilization influence the electronic structure and bonding environment, potentially enhancing charge carrier mobility and interfacial charge transfer dynamics. The SEM images support these findings, revealing a transition from agglomerated TiO_2 nanoparticles to a smoother, well-integrated nanocomposite film, confirming the formation of a refined hybrid structure with improved material homogeneity and interfacial interactions.

The SEM images (Figure 1c) illustrate the morphological transformation from agglomerated TiO_2-NPs to a smooth and compact $TiO_2/(MA)_2SnCl_4$ nanocomposite film, confirming structural modifications induced by Sn and MA incorporation. The TiO_2-NPs exhibit a rough, highly agglomerated morphology with loosely packed particles and visible voids, corresponding to the sharp anatase Raman peaks (144, 197, 396, 515, and 640 cm^{-1}), which indicate high crystallinity. As MA and $SnCl_2$ are introduced, the middle-stage sample displays reduced agglomeration and enhanced particle connectivity, signifying initial interactions between TiO_2, MA, and Sn, which are reflected in Raman peak broadening in the 144–640 cm^{-1} range, indicative of lattice distortions and TiO_2 encapsulation effects.

The final $TiO_2/(MA)_2SnCl_4$ nanocomposite exhibits a uniform, dense, and well-organized film-like structure, confirming successful TiO_2 encapsulation within the $(MA)_2SnCl_4$ matrix, as supported by weakened TiO_2 Raman peaks and the emergence of new organic vibrational modes in the 1000–3500 cm^{-1} region. These morphological refinements indicate improved material homogeneity, enhanced interfacial interactions, and better charge transport dynamics, making the nanocomposite an ideal candidate for photocatalytic and optoelectronic applications. The combined findings from SEM and Raman spectroscopy validate that Sn incorporation and MA stabilization lead to a structurally refined hybrid system with superior functional properties.

The XPS data in Figure 2 provides crucial insights into the elemental composition, chemical states, and interactions in the $TiO_2/(MA)_2SnCl_4$ nanocomposite film compared to the TiO_2-NPs film. The survey scan (Figure 2a) confirms the successful incorporation of Sn, Cl, C, N, and O in the nanocomposite, indicating the effective integration of the $(MA)_2SnCl_4$ phase into the TiO_2-NPs matrix. In contrast, the TiO_2-NPs spectrum primarily shows Ti and O, with a small C 1s peak attributed to surface contamination. The additional peaks for Sn 4d, Cl 2p, N 1s, Sn 3d, and Sn 3p in the nanocomposite confirm that Sn, MA, and Cl have effectively interacted with TiO_2, forming a stable hybrid structure even after sunlight exposure.

Figure 2b presents the high-resolution XPS spectra for the N 1s, Cl 2p, and Sn 3d regions, further verifying the integration of $(MA)_2SnCl_4$ into the TiO_2 framework. The N 1s spectrum exhibits three distinct peaks: N1 (398.2 eV), corresponding to nitrogen in a reduced environment (likely associated with MA^+) [26,27], N2 (398.8 eV), attributed to nitrogen involved in hydrogen bonding or interaction with TiO_2 surface groups; and N3 (401.5 eV), linked to nitrogen in a more oxidized environment. The Cl 2p spectrum shows two characteristic peaks, Cl $2p_3/_2$ (201.7 eV) and Cl $2_{p1}/_2$ (199.9 eV), confirming the presence of chloride ions from the $(MA)_2SnCl_4$ phase [28]. The Sn 3d spectrum deconvolutes into two pairs of peaks, corresponding to Sn^{2+} (485.4 eV for Sn $3d_5/_2$ and 494.0 eV for Sn $3d_3/_2$) and Sn^{4+} (486.8 eV for Sn $3d_5/_2$ and 495.7 eV for Sn $3d_3/_2$), confirming the coexistence of multiple oxidation states [29]. This suggests partial oxidation of Sn^{2+} to

Sn^{4+} during synthesis, likely facilitated by sunlight exposure and atmospheric oxygen, which could impact the material's optoelectronic properties. The combined evidence from the N 1s, Cl 2p, and Sn 3d spectra strongly supports the formation of an $(MA)_2SnCl_4$-based hybrid material, effectively encapsulating the TiO_2-NPs and modifying its surface chemistry. These modifications are expected to enhance interfacial charge transfer and improve the nanocomposite's stability and functional performance in photocatalytic and optoelectronic applications.

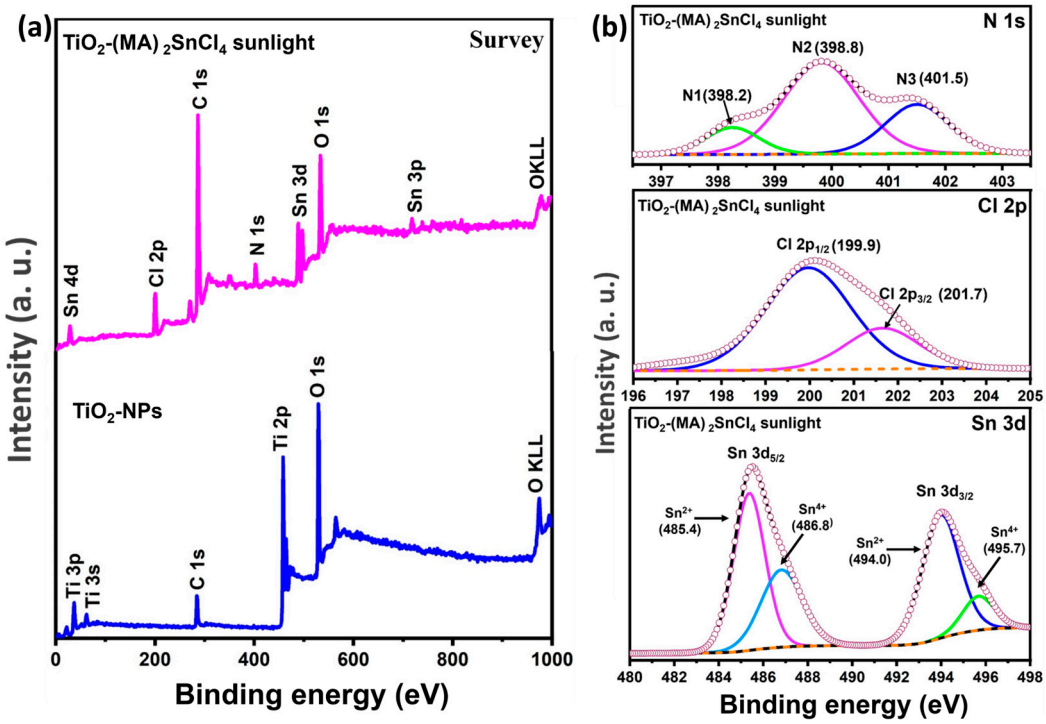


Figure 2. XPS analysis of TiO_2-NPs film and $TiO_2/(MA)_2SnCl_4$ film after sunlight exposure. (**a**) Survey spectra showing Ti, O, C, Sn, Cl, and N. (**b**) High-resolution XPS spectra of N 1s, Cl 2p, and Sn 3d, confirming chemical states and bonding in $TiO_2/(MA)_2SnCl_4$ nanocomposite post-exposure.

The XPS data in Figure 3 compares the C 1s, Ti 2p, and O 1s core-level spectra for TiO_2-NPs and $TiO_2/(MA)_2SnCl_4$ nanocomposite films after sunlight exposure, providing insights into the chemical bonding, surface interactions, and modifications induced by incorporating the $(MA)_2SnCl_4$ phase into TiO_2-NPs. As shown in Figure 3a, both TiO_2-NPs and the nanocomposite exhibit three main C 1s peaks [30,31]: C1 (284.5 eV), attributed to adventitious carbon from surface contamination, corresponding to C–C or C–H bonds; C2 (286.0 eV), associated with C–O or C–OH bonds, likely resulting from atmospheric exposure; and C3 (288.3 eV), representing higher oxidation states of carbon (C=O or O=C–O bonds), possibly from adsorbed CO_2. In the $TiO_2/(MA)_2SnCl_4$ nanocomposite, the C 1s spectrum exhibits a shift to lower binding energies and the emergence of additional carbon environments, confirming the presence of the methylammonium (MA) group. The C1 peak shifts slightly to 284.0 eV, corresponding to C–C or C–H bonds, likely originating from the organic MA group. A new C2 peak at 285.6 eV, attributed to C–N bonds, confirms the incorporation of the MA cation into the nanocomposite [32,33]. The C3 peak remains at 288.3 eV, reflecting oxidized carbon species (C=O or O=C–O), which may arise from surface oxidation or partial degradation under sunlight exposure. These spectral modifications suggest that MA integration significantly alters the nanocomposite's surface chemistry, enhancing interfacial interactions and modifying the electronic environment, which may contribute to improved photocatalytic and optoelectronic properties.

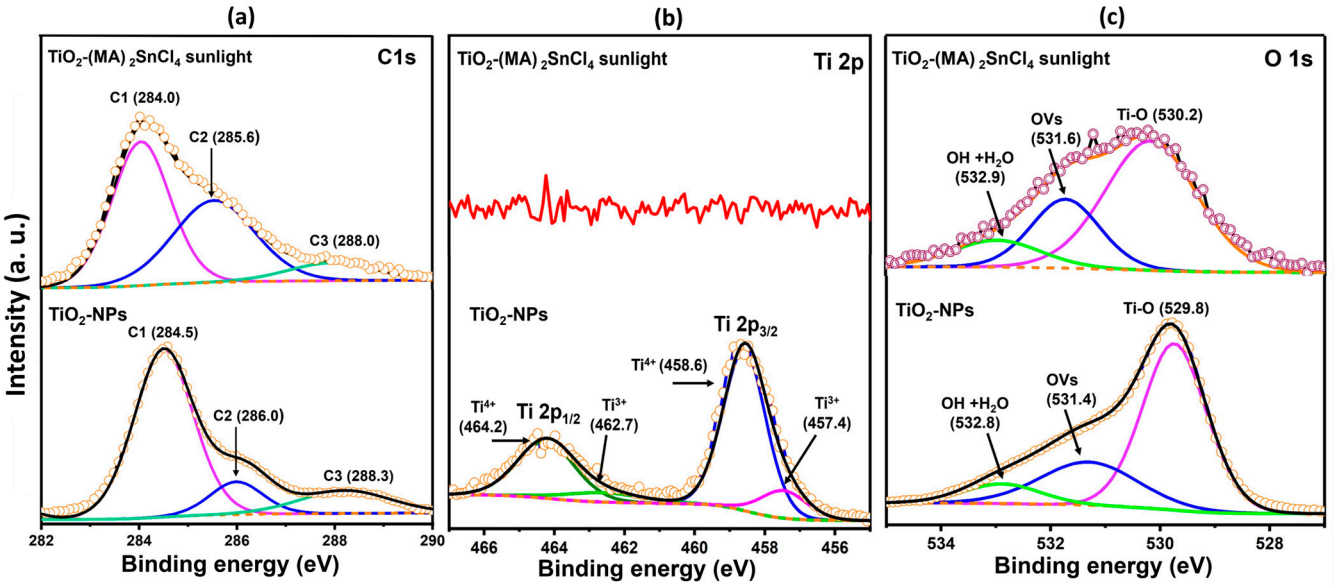


Figure 3. High-resolution XPS spectra of (**a**) C 1s, (**b**) Ti 2p, and (**c**) O 1s for TiO_2-NPs film and $TiO_2/(MA)_2SnCl_4$ film after sunlight exposure, showing changes in carbon bonding, titanium oxidation states, and OVs in samples.

In the TiO_2-NPs (Figure 3b), the Ti 2p spectrum exhibits two distinct peaks for Ti $2p_3/_2$, with a dominant peak at 458.6 eV corresponding to Ti^{4+} in the anatase phase, and a secondary peak at 457.4 eV, attributed to Ti_{3+}, indicating the presence of intrinsic lattice defects associated with oxygen vacancies (OVs), which are known to enhance photocatalytic activity. Additional peaks for Ti $2_{p1}/_2$ at 464.2 eV (Ti^{4+}) further confirm the presence of titanium in its oxidized state, while the peak at 462.7 eV (Ti_{3+}) signifies titanium in a reduced state, reinforcing the existence of OVs and defect-induced electronic states in TiO_2 [34]. In contrast, the Ti 2p signal is notably absent in the $TiO_2/(MA)_2SnCl_4$ nanocomposite, indicating complete encapsulation of TiO_2 by the $(MA)_2SnCl_4$ phase. This encapsulation effectively masks the TiO_2 core from detection, supporting the formation of a uniform hybrid coating that integrates the nanocomposite's components and influences its surface chemistry [35,36].

The O 1s spectrum (Figure 3c) provides further insights into the oxygen environment of both TiO_2-NPs and $TiO_2/(MA)_2SnCl_4$ nanocomposite after sunlight exposure. In TiO_2-NPs, the peak at 529.8 eV corresponds to lattice oxygen (Ti–O bonds) in the anatase crystal structure [37], eflecting a highly ordered lattice with minimal defects. However, in the nanocomposite, this peak shifts slightly to 530.2 eV with reduced intensity, suggesting lattice reorganization due to $(MA)_2SnCl_4$ integration. A peak at 531.4 eV in TiO_2-NPs, associated with defective oxygen sites due to intrinsic lattice defects [38,39], shifts to 531.6 eV in the nanocomposite, with a significant increase in intensity, confirming a higher concentration of OVs. This increase in OVs can be attributed to the dual oxidation states of Sn (Sn^{2+} and Sn^{4+}), which play a critical role in defect formation.

The presence of Sn^{2+} and Sn^{4+} in the nanocomposite promotes oxygen vacancy generation through a charge compensation mechanism. Sn^{2+}, with a lower oxidation state than Ti^{4+}, induces local charge imbalance when substituting Ti sites, leading to oxygen vacancy formation to maintain charge neutrality. Additionally, the partial oxidation of Sn^{2+} to Sn^{4+} during synthesis or sunlight exposure causes the release of lattice oxygen, further increasing the concentration of OVs. These vacancies play a crucial role in facilitating charge separation, reducing electron–hole recombination, and improving overall electronic conductivity, contributing to enhanced functionality. The peak at ~532.8 eV, corresponding

to surface hydroxyl groups or adsorbed water, is intensified and broadened in the nanocomposite, indicating an increase in hydroxyl species and adsorbed moisture, which enhances surface reactivity and catalytic performance [40].

The notable rise in OVs and surface defects in the $TiO_2/(MA)_2SnCl_4$ nanocomposite after sunlight exposure suggests structural modifications that contribute to improved charge transport, interfacial charge transfer, and electronic interactions [41]. These observations highlight the profound structural and electronic changes induced by Sn^{2+} and Sn^{4+} incorporation, supporting the formation of a refined hybrid system with enhanced functional properties.

The synthesis of the $TiO_2/(MA)_2SnCl_4$ nanocomposite film (Figure 4) involves a series of chemical interactions and sunlight-driven transformations, ensuring the successful integration of Sn, MA, and TiO_2 into a hybrid structure. Initially, TiO_2 nanoparticles (TiO_2-NPs) are dispersed in ethanol to create a stable colloidal suspension, where ethanol prevents agglomeration by forming hydrogen bonds with surface hydroxyl groups on TiO_2, promoting uniform dispersion. This suspension is then mixed with a precursor solution of methylammonium chloride (MA) and $SnCl_2$, facilitating initial interactions between Sn^{2+} ions and TiO_2 surfaces. The mixture is drop-cast onto a clean glass substrate and dried under ambient conditions, allowing ethanol evaporation, which concentrates MA^+ and Sn ions around TiO_2-NPs, promoting further interactions and nucleation. The dry film is then exposed to direct sunlight for 2 h, utilizing solar energy to drive photochemical reactions and oxidation processes.

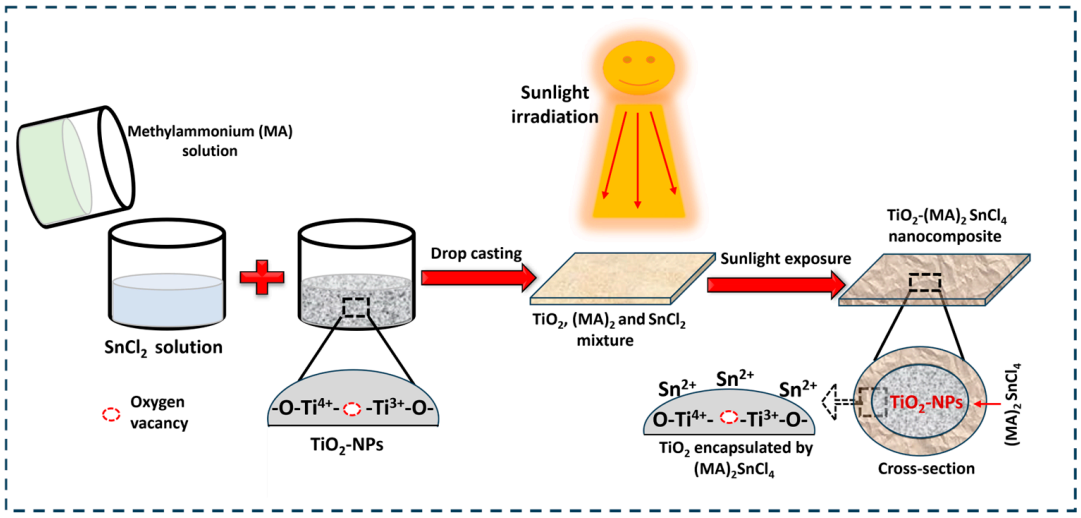


Figure 4. A schematic illustration of the synthesis mechanism for the TiO_2-$(MA)_2SnCl_4$ nanocomposite film under sunlight exposure, highlighting the encapsulation of TiO_2-NPs by the $(MA)_2SnCl_4$.

During the synthesis process, $SnCl_2$ undergoes oxidation and hydrolysis, where Sn^{2+} is partially oxidized to Sn^{4+} due to interactions with photogenerated charge carriers in TiO_2, with holes driving the oxidation reaction. Atmospheric oxygen further facilitates Sn^{2+} to Sn^{4+} conversion, leading to an increased Sn^{2+}/Sn^{4+} ratio, which enhances OVs formation [42]. The coexistence of Sn^{2+} and Sn^{4+} generates OVs in TiO_2, which serve as active sites for charge transport and electronic interactions. In the nanocomposite, Sn–O bonds dominate, forming strong covalent or ionic linkages between Sn^{4+} and oxygen atoms on TiO_2, including lattice oxygen and hydroxyl groups, ensuring structural stability and efficient charge transfer, while MA^+ interacts through hydrogen bonding and electrostatic forces.

Unlike a simple surface modification, TiO_2 is embedded within the composite, forming a well-integrated hybrid structure. This Sn–O-Ti interaction optimizes charge carrier

dynamics, facilitating electron transfer from $(MA)_2SnCl_4$ to TiO_2 while holes migrate in the opposite direction, reducing charge recombination. The presence of OVs stabilizes this heterostructure, enhancing charge mobility and improving photocatalytic efficiency. This synergistic interaction between TiO_2, Sn species, and MA significantly enhances light absorption and charge separation, making the nanocomposite highly effective for photoactive applications [43].

Figure 5 presents the optical properties of TiO_2-NPs and $TiO_2/(MA)_2SnCl_4$ nanocomposite films, comparing their absorbance spectra and Tauc plots for band gap estimation. Figure 5a shows that the TiO_2-NPs film exhibits an absorption edge at approximately 386 nm [30], corresponding to a band gap energy of ~3.1 eV, which is characteristic of UV-light-active TiO_2-NPs. In contrast, the $TiO_2/(MA)_2SnCl_4$ nanocomposite demonstrates a red-shifted absorption edge, extending into the visible region up to ~480 nm. This enhanced visible-light absorption results from the incorporation of Sn and MA, which introduce intermediate electronic states within the band gap, modifying the optical transition pathways [44]. The Tauc plots (Figure 5b) reveal a band gap reduction from 3.1 eV in TiO_2-NPs to approximately 2.6 eV in the nanocomposite, attributed to defect engineering and structural modifications.

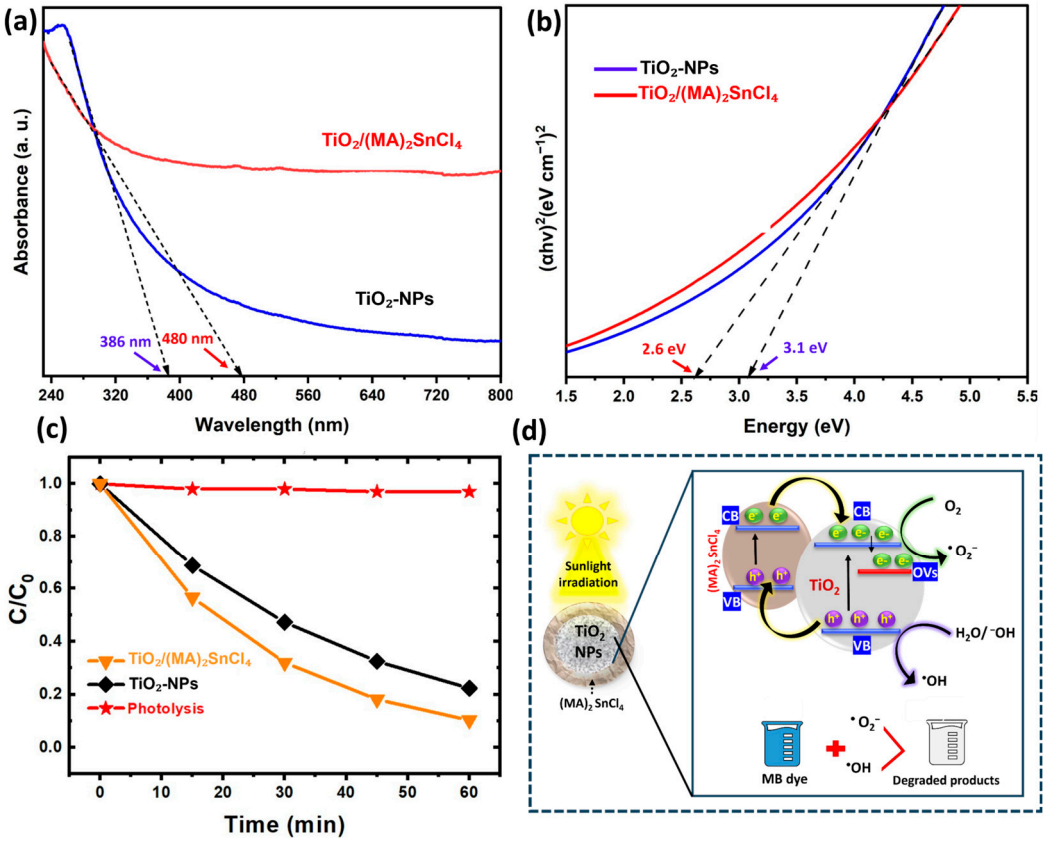


Figure 5. An overview of the optical properties and photocatalytic performance of TiO_2-NPs film and TiO_2-$(MA)_2SnCl_4$ nanocomposite film. (**a**) UV-Vis absorbance spectra showing the extended absorption edge of TiO_2-$(MA)_2SnCl_4$ towards the visible region. (**b**) Tauc plots indicating band gap reduction in the nanocomposite. (**c**) The degradation of MB under sunlight, showing the superior photocatalytic efficiency of TiO_2-$(MA)_2SnCl_4$ film compared to TiO_2-NPs film and photolysis. (**d**) The proposed mechanism illustrating improved charge separation and electron transfer between TiO_2-NPs film and $(MA)_2SnCl_4$, facilitated by the heterojunction structure.

The presence of Sn^{2+} and Sn^{4+} induces OVs, which introduce additional electronic states within the TiO_2 band gap, effectively narrowing the band gap and improving visible-

light absorption. The broader absorbance spectrum observed in the nanocomposite, compared to TiO_2-NPs, signifies improved light-harvesting capabilities, particularly in the visible range, which is advantageous for photocatalytic applications by enabling more efficient utilization of solar energy. The enhanced absorption is further supported by the formation of OVs during sunlight exposure [36,39], which generate localized energy levels, extending light absorption into the visible region and acting as active sites for catalytic reactions [39]. This combination of band gap narrowing, defect engineering, and extended absorption range significantly enhances the photocatalytic efficiency of the nanocomposite, making it a promising material for solar-driven applications.

The photocatalytic efficiency of TiO_2-NPs and $TiO_2/(MA)_2SnCl_4$ nanocomposite films was evaluated using methylene blue (MB) dye degradation under direct sunlight, assessing their ability to facilitate photodegradation. The TiO_2-NPs film exhibited moderate performance, achieving 75% MB degradation within 60 min, primarily due to its UV-light absorption, enabled by its band gap of 3.1 eV. In contrast, the $TiO_2/(MA)_2SnCl_4$ nanocomposite demonstrated superior photocatalytic activity, reaching 90% MB degradation within the same timeframe. Figure 5c highlights this enhanced efficiency, showing that the nanocomposite significantly outperforms TiO_2-NPs and the control experiment (photolysis without a catalyst), which exhibited negligible MB degradation, confirming the critical role of the photocatalyst in effective sunlight-driven degradation.

The improved photocatalytic performance of the $TiO_2/(MA)_2SnCl_4$ nanocomposite can be attributed to several key factors: (1) The incorporation of Sn and MA modifies the electronic structure, extending light absorption into the visible region and reducing the band gap to ~2.6 eV, enabling better solar energy utilization; (2) The formation of a Sn–O–Ti interaction within the nanocomposite facilitates charge transfer and efficient charge separation, minimizing electron–hole recombination and increasing the number of reactive charge carriers; and (3) The generation of OVs during sunlight exposure serves as active sites and electron traps, further enhancing photocatalytic activity by promoting interfacial charge transfer and surface redox reactions [45,46]. This synergistic combination of extended light absorption, effective charge separation, and active defect sites makes $TiO_2/(MA)_2SnCl_4$ a highly efficient material for solar-driven environmental remediation, offering significant advantages over conventional TiO_2-based photocatalysts.

The enhanced photocatalytic performance of the $TiO_2/(MA)_2SnCl_4$ nanocomposite, as illustrated in Figure 5d, results from a combination of synergistic effects, including extended light absorption, efficient charge separation, and structural modifications induced by sunlight exposure. The formation of Sn–O–Ti interactions within the nanocomposite facilitates strong interfacial bonding, significantly reducing the band gap to 2.6 eV compared to 3.1 eV for TiO_2-NPs. This reduction expands the absorption spectrum into the visible range, increasing the generation of photogenerated electron–hole pairs under solar irradiation. Upon sunlight exposure, both TiO_2 and Sn-containing species absorb photons, leading to electron excitation from the valence band to the conduction band, enabling efficient photocatalytic activity [20,21].

The band alignment between TiO_2 and Sn-containing phases promotes efficient charge transfer, where photoexcited electrons migrate to the conduction band of TiO_2, while holes move in the opposite direction, effectively minimizing recombination losses. This directional charge migration is driven by an internal electric field at the interface, a phenomenon observed in heterojunction-based photocatalysts such as S-scheme catalysts (e.g., N-doped CeO_2-δ@$ZnIn_2S_4$ and $TiO_2/g\text{-}C_3N_4$ heterojunctions) [47,48]. The internal charge redistribution ensures higher availability of charge carriers, which participate in surface redox reactions critical for pollutant degradation [45,46].

Furthermore, OVs generated during sunlight exposure play a pivotal role in enhancing charge carrier dynamics. These OVs serve as electron traps, further reducing electron–hole recombination, while also introducing intermediate states within the band gap, improving visible light absorption and adsorption of oxygen molecules and organic pollutants. During the photocatalytic reaction, photoexcited electrons in the TiO_2 conduction band reduce O_2 to superoxide radicals ($^{\bullet}O_2^-$), while holes in the valence band oxidize water or hydroxyl groups to generate hydroxyl radicals ($^{\bullet}OH$). These highly reactive species drive the degradation of pollutants such as MB, facilitating efficient photocatalytic performance.

The synergistic combination of band gap reduction, heterojunction-driven charge separation, OVs formation, and efficient reactive oxygen species (ROS) generation explains the superior photocatalytic activity of the $TiO_2/(MA)_2SnCl_4$ nanocomposite. These interactions enable the nanocomposite to outperform pure TiO_2 in organic pollutant degradation under sunlight, aligning with recent heterostructure-based charge transfer mechanisms that enhance photocatalytic efficiency.

3. Method Preparation and Characterization

3.1. Materials

The materials used in this study were utilized as received without any further purification. Titanium dioxide nanoparticles (TiO_2-NPs) were sourced as commercial TiO_2 P25 (99.5%, Evonik, Mount Waverley, VIC, Australia), known for exhibiting a small number of intrinsic defects. Methylammonium chloride (MA) (99%, Sigma-Aldrich, St. Louis, MO, USA), tin(II) chloride ($SnCl_2$) ($\geq$98%, Sigma-Aldrich, St. Louis, MO, USA), hydrochloric acid (HCl, 37%, Fisher Scientific, Hampton, NH, USA), and ethanol ($\geq$99.8%, Sigma-Aldrich, St. Louis, MO, USA) were also employed in the synthesis and preparation processes.

3.2. Preparation of MA and $SnCl_2$ Mixture

MA and $SnCl_2$ were dissolved in ethanol to prepare the precursor solution, maintaining a molar ratio of 2:1 for MA to $SnCl_2$. Before dissolving MA, HCl was added to the MA solution. This step was performed carefully to prevent over-acidification, ensuring that only a stoichiometric amount of HCl was used. After that, the $SnCl_2$ solution was added to the MA solution to form the MA and $SnCl_2$ mixture.

3.3. Synthesis of $TiO_2/(MA)_2SnCl_4$ Nanocomposite Film

TiO_2-NPs were dispersed in ethanol to form a stable colloidal suspension, which was then mixed with a 20% solution of MA and $SnCl_2$ precursor mixture at a 0.454:1 volume ratio. This mixture was drop-cast onto a pre-cleaned glass substrate and allowed to evaporate under ambient conditions, forming a uniform thin film. The resulting films were exposed to direct sunlight for 2 h to facilitate the reaction between MA and $SnCl_2$, resulting in the formation of $(MA)_2SnCl_4$ and the synthesis of the $TiO_2/(MA)_2SnCl_4$ nanocomposite film. This sunlight exposure was carried out under midday conditions in Al-Kharj City, Saudi Arabia. After sunlight exposure, the films were washed with ethanol to remove any unreacted precursors and dried under ambient conditions.

3.4. Characterization

The Raman spectroscopy was conducted using a SENTERRA II Compact Raman Microscope (Houston, TX, USA) with a 532 nm laser (2 mW power, 1 cm^{-1} resolution) to identify the vibrational modes of TiO_2-NPs and $TiO_2/(MA)_2SnCl_4$ films, providing insights into structural modifications and chemical interactions. Scanning electron microscopy (SEM) was performed with an FEI Quanta 250 instrument (Hillsboro, OR, USA) to examine surface morphology and nanoparticle distribution, revealing changes in film uniformity

and particle agglomeration. Elemental composition and chemical states were analyzed through X-ray photoelectron spectroscopy (XPS) using a Thermo Scientific K-alpha system (Waltham, MA, USA) with an Al Kα source (1486.6 eV, 400 μm spot size), employing C 1s (284.5 eV) for charge correction to ensure accurate binding energy calibration. UV-Vis spectroscopy, conducted with a UV-5200 spectrophotometer (Shanghai Xiwen Biotech Co., Ltd., Shanghai, China), was used to assess the optical absorption properties of the films, evaluating their light-harvesting efficiency and band gap modifications.

3.5. Photocatalytic Performance Method

A 5 ppm aqueous solution of methylene blue (MB), used as a model organic pollutant, was prepared and placed in a stationary photocatalytic reactor and a magnetic stirrer set to 300 r.p.m. The $TiO_2/(MA)_2SnCl_4$ films, each with an area of 4 cm^2, were submerged 2 mm deep in 10 mL of the MB solution. To ensure adsorption/desorption equilibrium, the setup was kept in the dark for 30 min prior to sunlight exposure. The reactor was then exposed to direct sunlight, and control experiments using TiO_2-NPs films and no catalyst were conducted for comparison. Each experiment was repeated at least three times for reproducibility. Photocatalytic tests were carried out in midday sunlight in Al-Kharj City, Saudi Arabia. Samples were collected every 15 min during irradiation, and the concentration of MB was analyzed using UV-Vis spectroscopy by recording absorbance at 665 nm. The degradation efficiency was calculated using the following formula:

$$\text{Degradation efficiency (\%)} = (C_0 - C/C_0) \times 100$$

where C_0 is the initial concentration of the pollutant and C is the concentration at time t. This approach enabled a detailed comparison of the photocatalytic performance between the TiO_2-NPs and $TiO_2/(MA)_2SnCl_4$ films.

4. Conclusions

The $TiO_2/(MA)_2SnCl_4$ nanocomposite film developed in this study demonstrates significant advancements in photocatalytic performance, making it a promising material for water purification applications. The enhanced photocatalytic activity is attributed to the effective integration of Sn and MA components into the TiO_2-NPs framework, leading to extended light absorption into the visible region and improved charge separation via strong Sn–O–Ti interactions. UV-Vis spectroscopy confirmed a substantial band gap reduction from 3.1 eV in TiO_2-NPs to approximately 2.6 eV in the nanocomposite, improving visible-light utilization. XPS analysis further revealed the critical role of OVs, which facilitated charge trapping, minimized recombination, and enhanced catalytic efficiency. The $TiO_2/(MA)_2SnCl_4$ nanocomposite film achieved ~90% degradation of MB dye under sunlight within 60 min, outperforming the TiO_2-NPs film, which achieved only 75% degradation, underscoring the effectiveness of defect engineering and interfacial charge transfer. The synergistic effects of structural modification, optimized charge dynamics, and defect-mediated electronic interactions contribute to the nanocomposite's superior photocatalytic efficiency. The use of sunlight as a renewable energy source enhances sustainability, making this approach not only cost-effective and scalable but also a viable solution for addressing global water contamination challenges. These findings demonstrate that rational material design, incorporating controlled structural and electronic modifications, can significantly improve photocatalytic performance, paving the way for advanced environmental remediation technologies.

Author Contributions: Conceptualization, A.K. and T.F.Q.; Methodology, A.K. and A.M.A.; Software, A.O. and S.T.H.; Validation, N.A., S.T.H. and A.O.; Formal Analysis, A.M.A. and A.O.; Investigation, A.K., A.M.A. and N.A.; Resources, I.C.; Data Curation, I.C., S.T.H. and M.R.; experimental support, I.C.; experimental analysis, N.A.; Writing—Original Draft, A.K. and A.M.A.; Writing—Review and Editing, S.T.H., M.R. and T.F.Q.; Project Administration, T.F.Q.; Funding Acquisition, T.F.Q. All authors have read and agreed to the published version of the manuscript.

Funding: This project is sponsored by Prince Sattam Bin Abdulaziz University (PSAU) as a part of the funding for its SDG Roadmap Research Funding Programme project number PSAU-2023-SDG-94.

Data Availability Statement: Data are contained within the article.

Conflicts of Interest: The authors declare no conflict of interest.

References

1. Bolisetty, S.; Peydayesh, M.; Mezzenga, R. Sustainable Technologies for Water Purification from Heavy Metals: Review and Analysis. *Chem. Soc. Rev.* **2019**, *48*, 463–487. [CrossRef]
2. Ahmed, S.; Khan, F.S.A.; Mubarak, N.M.; Khalid, M.; Tan, Y.H.; Mazari, S.A.; Karri, R.R.; Abdullah, E.C. Emerging Pollutants and Their Removal Using Visible-Light Responsive Photocatalysis—A Comprehensive Review. *J. Environ. Chem. Eng.* **2021**, *9*, 106643. [CrossRef]
3. Mohamadpour, F.; Mohammad Amani, A. Photocatalytic Systems: Reactions, Mechanism, and Applications. *RSC Adv.* **2024**, *14*, 20609–20645. [CrossRef] [PubMed]
4. Mohapatra, L.; Yoo, S.H. Superwetting Materials as Catalysts in Photocatalysis: State-of-the-Art Review. *Chem. Eng. J.* **2024**, *481*, 148537. [CrossRef]
5. Chakravorty, A.; Roy, S. A Review of Photocatalysis, Basic Principles, Processes, and Materials. *Sustain. Chem. Environ.* **2024**, *8*, 100155. [CrossRef]
6. Armaković, S.J.; Savanović, M.M.; Armaković, S. Titanium Dioxide as the Most Used Photocatalyst for Water Purification: An Overview. *Catalysts* **2023**, *13*, 26. [CrossRef]
7. Dharma, H.N.C.; Jaafar, J.; Widiastuti, N.; Matsuyama, H.; Rajabsadeh, S.; Othman, M.H.D.; Rahman, M.A.; Jafri, N.N.M.; Suhaimin, N.S.; Nasir, A.M.; et al. A Review of Titanium Dioxide (TiO_2)-Based Photocatalyst for Oilfield-Produced Water Treatment. *Membranes* **2022**, *12*, 345. [CrossRef]
8. Lettieri, S.; Pavone, M.; Fioravanti, A.; Santamaria Amato, L.; Maddalena, P. Charge Carrier Processes and Optical Properties in TiO_2 and TiO_2-Based Heterojunction Photocatalysts: A Review. *Materials* **2021**, *14*, 1645. [CrossRef] [PubMed]
9. Magalhães, P.; Andrade, L.; Nunes, O.; Mendes, A. Titanium Dioxide Photocatalysis: Fundamentals and Application on Photoinactivation. *Rev. Adv. Mater. Sci.* **2017**, *51*, 91–129.
10. Du, S.; Lian, J.; Zhang, F. Visible Light-Responsive N-Doped TiO_2 Photocatalysis: Synthesis, Characterizations, and Applications. *Trans. Tianjin Univ.* **2022**, *28*, 33–52. [CrossRef]
11. Etacheri, V.; Di Valentin, C.; Schneider, J.; Bahnemann, D.; Pillai, S.C. Visible-Light Activation of TiO_2 Photocatalysts: Advances in Theory and Experiments. *J. Photochem. Photobiol. C Photochem. Rev.* **2015**, *25*, 1–29. [CrossRef]
12. Khan, H.; Shah, M.U.H. Modification Strategies of TiO_2 Based Photocatalysts for Enhanced Visible Light Activity and Energy Storage Ability: A Review. *J. Environ. Chem. Eng.* **2023**, *11*, 111532. [CrossRef]
13. Wajid Shah, M.; Zhu, Y.; Fan, X.; Zhao, J.; Li, Y.; Asim, S.; Wang, C. Facile Synthesis of Defective TiO_{2-x} Nanocrystals with High Surface Area and Tailoring Bandgap for Visible-Light Photocatalysis. *Sci. Rep.* **2015**, *5*, 15804. [CrossRef]
14. Wang, C.; Ding, Y.; Wang, Y.; Xie, Z.; Zeng, Z.; Li, X.; Ng, Y.H. Metal Halide Perovskites for Solar-to-Chemical Energy Conversion in Aqueous Media. *Carbon Energy* **2024**, *6*, e500. [CrossRef]
15. Purohit, S.; Yadav, K.L.; Satapathi, S. Metal Halide Perovskite Heterojunction for Photocatalytic Hydrogen Generation: Progress and Future Opportunities. *Adv. Mater. Interfaces* **2022**, *9*, 2200058. [CrossRef]
16. Mortan, C.; Hellmann, T.; Buchhorn, M.; Melzi d'Eril, M.; Clemens, O.; Mayer, T.; Jaegermann, W. Preparation of Methylammonium Lead Iodide ($CH_3NH_3PbI_3$) Thin Film Perovskite Solar Cells by Chemical Vapor Deposition Using Methylamine Gas (CH_3NH_2) and Hydrogen Iodide Gas. *Energy Sci. Eng.* **2024**, *8*, 3165–3173. [CrossRef]
17. Quarti, C.; Mosconi, E.; Ball, J.M.; D'Innocenzo, V.; Tao, C.; Pathak, S.; Snaith, H.J.; Petrozza, A.; Angelis, F.D. Structural and Optical Properties of Methylammonium Lead Iodide across the Tetragonal to Cubic Phase Transition: Implications for Perovskite Solar Cells. *Energy Environ. Sci.* **2016**, *9*, 155–163. [CrossRef]
18. Pan, L.; Feng, Y.; Kandlakunta, P.; Huang, J.; Cao, L.R. Performance of Perovskite CsPbBr3 Single Crystal Detector for Gamma-Ray Detection. *IEEE Trans. Nucl. Sci.* **2020**, *67*, 443–449. [CrossRef]

19. Baloch, A.; Hossain, M.; Tabet, N.; Alharbi, F. Practical Efficiency Limit of Methylammonium Lead Iodide Perovskite ($CH_3NH_3PbI_3$) Solar Cells. *J. Phys. Chem. Lett.* **2018**, *9*, 426–434. [CrossRef] [PubMed]
20. Cuzzupè, D.; Öz, S.; Ling, J.-K.; Illing, E.; Seewald, T.; Jose, R.; Olthof, S.; Fakharuddin, A.; Schmidt-Mende, L. Understanding Methylammonium Chloride-Assisted Crystallization for Improved Performance of Lead–Free Tin Perovskite Solar Cells. *Sol. RRL* **2023**, *7*, 2300770. [CrossRef]
21. Awais, M.; Kirsch, R.L.; Yeddu, V.; Saidaminov, M.I. Tin Halide Perovskites Going Forward: Frost Diagrams Offer Hints. *ACS Mater. Lett.* **2021**, *3*, 299–307. [CrossRef]
22. Kumar, A. Different Methods Used for the Synthesis of TiO_2 Based Nanomaterials: A Review. *Am. J. Nano Res. Appl.* **2018**, *6*, 1. [CrossRef]
23. Mani, S.S.; Rajendran, S.; Mathew, T.; Gopinath, S.C. A Review on the Recent Advances in the Design and Structure–Activity Relationship of TiO_2-Based Photocatalysts for Solar Hydrogen Production. *Energy Adv.* **2024**, *3*, 1472–1504. [CrossRef]
24. Khalid, A.; Ahmad, P.; Alharthi, A.; Muhammad, S.; Khandaker, M.; Faruque, M.R.; Faruque, I.; Din, I.U.; Alotaibi, M.; Kustov, L. Unmodified Titanium Dioxide Nanoparticles as a Potential Contrast Agent in Photon Emission Computed Tomography. *Crystals* **2021**, *11*, 171. [CrossRef]
25. Yadav, R.; Swain, D.; Kundu, P.P.; Nair, H.S.; Narayana, C.; Elizabeth, S. Dielectric and Raman Investigations of Structural Phase Transitions in $(C_2H_5NH_3)_2CdCl_4$. *Phys. Chem. Chem. Phys.* **2015**, *17*, 12207–12214. [CrossRef] [PubMed]
26. Tang, M.-C.; Zhang, S.; Magnanelli, T.; Nguyen, N.; Heilweil, E.; Anthopoulos, T.; Hacker, C. Unraveling the Compositional Heterogeneity and Carrier Dynamics of Alkali Cation Doped 3D/2D Perovskites with Improved Stability. *Mater. Adv.* **2020**, *2*, 1253–1262. [CrossRef]
27. Zhou, Q.; Liang, L.; Hu, J.; Cao, B.; Yang, L.; Wu, T.; Li, X.; Zhang, B.; Gao, P. High-Performance Perovskite Solar Cells with Enhanced Environmental Stability Based on a (p-FC6H4C2H4NH3)2[PbI4] Capping Layer. *Adv. Energy Mater.* **2019**, *9*, 1802595. [CrossRef]
28. Shao, Y.X.; Cai, Y.H.; Dong, D.; Wang, S.; Ang, S.G.; Xu, G.Q. Spectroscopic Study of Propargyl Chloride Attachment on Si(1 0 0) − 2 × 1. *Chem. Phys. Lett.* **2009**, *482*, 77–80. [CrossRef]
29. Bandara, R.M.I.; Jayawardena, K.D.G.I.; Adeyemo, S.O.; Hinder, S.J.; Smith, J.A.; Thirimanne, H.M.; Wong, N.C.; Amin, F.M.; Freestone, B.G.; Parnell, A.J.; et al. Tin(IV) Dopant Removal through Anti-Solvent Engineering Enabling Tin Based Perovskite Solar Cells with High Charge Carrier Mobilities. *J. Mater. Chem. C* **2019**, *7*, 8389–8397. [CrossRef]
30. Alotaibi, M.A.; Alharthi, A.I.; Qahtan, T.F.; Alotibi, S.; Alansi, A.M.; Bakht, M.A. Photocatalytic Synthesis of Coumarin Derivatives Using Visible-Light-Responsive Strawberry Dye-Sensitized Titanium Dioxide Nanoparticles. *Catalysts* **2023**, *13*, 3001. [CrossRef]
31. Kang, S.; Mauchauffé, R.; You, Y.S.; Moon, S.Y. Insights into the Role of Plasma in Atmospheric Pressure Chemical Vapor Deposition of Titanium Dioxide Thin Films. *Sci. Rep.* **2018**, *8*, 16684. [CrossRef] [PubMed]
32. Chen, P.; Bai, Y.; Wang, S.; Lyu, M.; Yun, J.-H.; Wang, L. In Situ Growth of 2D Perovskite Capping Layer for Stable and Efficient Perovskite Solar Cells. *Adv. Funct. Mater.* **2018**, *28*, 1706923. [CrossRef]
33. Rocks, C.; Švrček, V.; Maguire, P.; Mariotti, D. Understanding Surface Chemistry during MAPbI 3 Spray Deposition and Its Effect on Photovoltaic Performance. *J. Mater. Chem. C* **2017**, *5*, 902–916. [CrossRef]
34. Xu, Y.; Wu, S.; Wan, P.; Sun, J.; Hood, Z. Introducing Ti^{3+} Defects Based on Lattice Distortion for Enhanced Visible Light Photoreactivity in TiO_2 Microspheres. *RSC Adv.* **2017**, *7*, 32461–32467. [CrossRef]
35. Li, Z.; Wang, S.; Wu, J.; Zhou, W. Recent Progress in Defective TiO_2 Photocatalysts for Energy and Environmental Applications. *Renew. Sustain. Energy Rev.* **2022**, *156*, 111980. [CrossRef]
36. Pan, X.; Yang, M.-Q.; Fu, X.; Zhang, N.; Xu, Y.-J. Defective TiO_2 with Oxygen Vacancies: Synthesis, Properties and Photocatalytic Applications. *Nanoscale* **2013**, *5*, 3601–3614. [CrossRef] [PubMed]
37. Yuan, Y.; Ji, Z.; Yan, G.; Li, Z.; Jinliang, L.; Kuang, M.; Jiang, B.; Zeng, L.; Pan, L.; Mai, W. TiO_2 Electron Transport Bilayer for All-Inorganic Perovskite Photodetectors with Remarkably Improved UV Stability toward Imaging Applications. *J. Mater. Sci. Technol.* **2021**, *75*, 39–47. [CrossRef]
38. Nguyen, D.; Ding, S.; Thuong, N.; Vân-Anh, N.; Mejía, E. Visible Light-Driven Degradation of Trichloroethylene in Aqueous Phase with Vanadium-Doped TiO 2 Photocatalysts. *Sol. RRL* **2023**, *7*. [CrossRef]
39. Guan, S.; Cheng, Y.; Hao, L.; Yoshida, H.; Tarashima, C.; Zhan, T.; Itoi, T.; Qiu, T.; Lu, Y. Oxygen Vacancies Induced Band Gap Narrowing for Efficient Visible-Light Response in Carbon-Doped TiO_2. *Sci. Rep.* **2023**, *13*, 14105. [CrossRef] [PubMed]
40. Chi, M.; Sun, X.; Lozano-Blanco, G.; Tatarchuk, B.J. XPS and FTIR Investigations of the Transient Photocatalytic Decomposition of Surface Carbon Contaminants from Anatase TiO_2 in UHV Starved Water/Oxygen Environments. *Appl. Surf. Sci.* **2021**, *570*, 151147. [CrossRef]
41. Alansi, A.M.; Qahtan, T.F.; Al Abass, N.; Al-Qunaibit, M.; Saleh, T.A. In-Situ Sunlight-Driven Tuning of Photo-Induced Electron-Hole Generation and Separation Rates in Bismuth Oxychlorobromide for Highly Efficient Water Decontamination under Visible Light Irradiation. *J. Colloid Interface Sci.* **2022**, *614*, 58–65. [CrossRef] [PubMed]

42. Bastug Azer, B.; Gulsaran, A.; Pennings, J.R.; Saritas, R.; Kocer, S.; Bennett, J.L.; Devdas Abhang, Y.; Pope, M.A.; Abdel-Rahman, E.; Yavuz, M. A Review: TiO_2 Based Photoelectrocatalytic Chemical Oxygen Demand Sensors and Their Usage in Industrial Applications. *J. Electroanal. Chem.* **2022**, *918*, 116466. [CrossRef]
43. Wang, Q.; Xiong, J.; Xing, Y.; Gan, X.; Zhu, W.; Xuan, R.; Liu, X.; Huang, L.; Zhu, Y.; Zhang, J. Reductive Sn Compensator for Efficient and Stable Sn-Pb Mixed Perovskite Solar Cells. *Adv. Sci.* **2024**, *11*, 2400962. [CrossRef] [PubMed]
44. Orudzhev, F.; Ramazanov, S.; Isaev, A.; Alikhanov, N.; Sobola, D.; Presniakov, M.Y.; Kaviyarasu, K. Self-Organization of Layered Perovskites on TiO_2 Nanotubes Surface by Atomic Layer Deposition. *Mater. Today Proc.* **2021**, *36*, 346–367. [CrossRef]
45. Yu, J.; Xiang, S.; Ge, M.; Zhang, Z.; Huang, J.; Tang, Y.; Sun, L.; Lin, C.; Lai, Y. Rational Construction of LaFeO3 Perovskite Nanoparticle-Modified TiO_2 Nanotube Arrays for Visible-Light Driven Photocatalytic Activity. *Coatings* **2018**, *8*, 374. [CrossRef]
46. Chen, C.; Zhou, J.; Geng, J.; Bao, R.; Wang, Z.; Xia, J.; Li, H. Perovskite $LaNiO_3/TiO_2$ Step-Scheme Heterojunction with Enhanced Photocatalytic Activity. *Appl. Surf. Sci.* **2020**, *503*, 144287. [CrossRef]
47. Farhan, S.; Hassan Raza, A.; Yang, S.; Yu, Z.; Wu, Y. Boosted Photocatalytic Hydrogen Evolution of S-Scheme N-Doped CeO2-δ@ZnIn2S4 Heterostructure Photocatalyst. *J. Colloid Interface Sci.* **2024**, *669*, 430–443. [CrossRef]
48. Yang, S.; Wang, K.; Chen, Q.; Wu, Y. Enhanced Photocatalytic Hydrogen Production of S-Scheme TiO_2/g-C3N4 Heterojunction Loaded with Single-Atom Ni. *J. Mater. Sci. Technol.* **2024**, *175*, 104–114. [CrossRef]

Disclaimer/Publisher's Note: The statements, opinions and data contained in all publications are solely those of the individual author(s) and contributor(s) and not of MDPI and/or the editor(s). MDPI and/or the editor(s) disclaim responsibility for any injury to people or property resulting from any ideas, methods, instructions or products referred to in the content.